

See discussions, stats, and author profiles for this publication at: <https://www.researchgate.net/publication/271600796>

Carrier mobility of MoS₂ nanoribbons with edge chemical modification

ARTICLE in PHYSICAL CHEMISTRY CHEMICAL PHYSICS · JANUARY 2015

Impact Factor: 4.49 · DOI: 10.1039/C4CP05199H

CITATION

1

READS

16

6 AUTHORS, INCLUDING:



Jin Xiao

Central South University

23 PUBLICATIONS 451 CITATIONS

SEE PROFILE



Xinmei Li

10 PUBLICATIONS 24 CITATIONS

SEE PROFILE



Hui Xu

Central South University

42 PUBLICATIONS 128 CITATIONS

SEE PROFILE



Kwok sum Chan

City University of Hong Kong

156 PUBLICATIONS 1,187 CITATIONS

SEE PROFILE



Cite this: *Phys. Chem. Chem. Phys.*,
2015, 17, 6865

Carrier mobility of MoS₂ nanoribbons with edge chemical modification

Jin Xiao,^a Mengqiu Long,^{*ab} Mingjun Li,^a Xinmei Li,^a Hui Xu^{*a} and Kwoksum Chan^{*bc}

We have investigated the electronic structures and carrier mobilities of MoS₂ monolayer sheets and armchair nanoribbons with chemical modification using the density functional theory combined with the Boltzmann transport method with relaxation time approximation. It is shown that the hole mobility (96.62 cm² V⁻¹ s⁻¹) in monolayer sheets is about twice that of the electron mobility (43.96 cm² V⁻¹ s⁻¹). The charge mobilities in MoS₂ armchair nanoribbons can be regulated by edge modification owing to the changing electronic structures. In pristine armchair nanoribbons, the electron and hole mobilities are about 30 cm² V⁻¹ s⁻¹ and 25 cm² V⁻¹ s⁻¹, respectively. When the edges are terminated by H or F atoms, the hole mobility will enhance obviously even 10 times that in pristine ribbons, and the electron mobility is comparable with that in MoS₂ sheets.

Received 10th November 2014,
Accepted 21st January 2015

DOI: 10.1039/c4cp05199h

www.rsc.org/pccp

Introduction

Two-dimensional, atomically thick materials have attracted intensive attention, owing to their unique physical properties and potential applications in nanoscale devices.^{1–9} In addition to layered transition-metal dichalcogenides (TMDs), which are important two-dimensional materials, MX₂ (M = Mo, W, Ta, or Nb, and X = S, Se, or Te) are also considered to be promising electronic and optoelectronic materials,^{9–15} and the successful syntheses of these materials have been previously reported.^{16–20} MoS₂, an important representative member of the TMD family, has aroused strong interest in the materials recently from many researchers.^{19–23} The monolayer MoS₂ is a direct band-gap semiconductor with a band gap of 1.9 eV,^{23,24} and the room-temperature current on/off ratio can be as high as 1×10^8 .¹³ Owing to the breaking of the inversion symmetry, a very obvious spin-orbit interaction effect is found around the high-symmetry *K*-points of the Brillouin zone with a spin-orbit splitting as high as 150 meV,^{25–27} according to some theoretical studies, and around 160 meV,^{28–31} according to some experimental studies. Utilizing this effect, the optical generation of valley polarization is achieved with the polarized photoluminescence technique in monolayer MoS₂.^{28–33}

Recently, the mobilities (μ) of two-dimensional materials have attracted the attention of numerous researchers.^{2,34–48}

Some measurements showed that the room-temperature mobility of bulk MoS₂ is in the range 200–500 cm² V⁻¹ s⁻¹.⁴³ The field effect mobility of atomically thin MoS₂ FET was reported to vary from 0.5 to 800 cm² V⁻¹ s⁻¹.^{13,44–48} By using a femto-second pump-probe technique to study the charge carriers, a carrier lifetime of 100 ± 10 picoseconds and a carrier diffusion coefficient of 20 ± 10 cm² s⁻¹ are obtained, which correspond to a mobility of 800 cm² V⁻¹ s⁻¹ and a diffusion length of 450 nm.⁴⁸ The presence of high-*K* dielectrics in some devices can enhance the mobilities⁴⁶ to values reaching ~ 200 cm² V⁻¹ s⁻¹.¹³ Radisavljevic and Kis⁴⁶ reported that phonon scattering shows a weaker-than-expected temperature dependence (μ follows a $T^{-\gamma}$ dependence with $\gamma = 0.55–0.78$) when temperatures reach above ~ 100 K, and the mobility at 4 K is 174 cm² V⁻¹ s⁻¹, and it reaches 63 cm² V⁻¹ s⁻¹ at 240 K.

By confinement of the two-dimensional bulk materials, one-dimensional materials can be created with different properties. For example, the carrier mobility of one-dimensional graphene ribbons is significantly lower than that of a graphene sheet, owing to the loss of the massless Dirac fermion characteristics.^{34,49} One-dimensional MoS₂ structures, such as nanoribbons⁵⁰ and nanotubes^{16–19} have also been synthesized, and the mobilities of these structures have attracted the attention of researchers.^{42,51} Nevertheless, there are few reports about the mobilities of MoS₂ nanoribbons with edge modification.

In this study, by using first-principles calculations and the deformation potential theory, we investigate the intrinsic mobility of MoS₂ materials due to the acoustic phonon scattering mechanism. The carrier mobility is calculated by the Boltzmann transport equation (BTE) method. The sheets and nanoribbons, particularly the chemical modifications on the ribbon's edges,

^a Institute of Super-microstructure and Ultrafast Process in Advanced Materials, School of Physics and Electronics, Central South University, Changsha 410083, China. E-mail: mqlong@csu.edu.cn, cmpxhg@csu.edu.cn

^b Department of Physics and Materials Science, City University of Hong Kong, Hong Kong, China. E-mail: apkschan@cityu.edu.hk

^c City University of Hong Kong Shenzhen Research Institute, Shenzhen, China

are considered in the calculations. Our results show that the electron structures and the mobilities of MoS₂ ribbons are sensitive to edge modification, and hydrogen atom termination will slightly change their mobility, whereas halogen atom termination will obviously enhance the hole mobility (μ_h). This implies that the electronic properties and mobilities of MoS₂ nanoribbons can be regulated by chemical modification.

Methods

Theoretically, there are two models for charge transport: hopping and band-like. The former describes the thermally activated hopping of a charge carrier over a barrier resulting in a mobility, which increases with temperature, owing to increased thermal activation. The hopping model has been described by the Marcus theory for many organic materials. The latter model describes a delocalized charge undergoing coherent motion resulting in a mobility, which decreases with temperature, owing to increased phonon scattering.^{38,52} Experiments find that the mobility of MoS₂ sheets decrease with temperature.⁴⁶ Thus, the band-like model is more appropriate in MoS₂ than the Marcus electron-transfer theory. Our method is based on the band-like model.

In this paper, the carrier mobility is calculated by the BTE method beyond the effective mass approximation, which is used to predict the mobility of semiconductor nanomaterials, such as graphene and carbon nanotubes, among others.^{2,34–38} Within the BTE method, the carrier mobility μ in the relaxation time approximation can be expressed as [ref. 2 and 54].

$$\mu^{e(h)} = \frac{e}{k_B T} \frac{\sum_{i \in \text{CB(VB)}} \int \tau(i, \vec{k}) v^2(i, \vec{k}) \exp\left[\mp \frac{\varepsilon_i(\vec{k})}{k_B T}\right] d\vec{k}}{\sum_{i \in \text{CB(VB)}} \int \exp\left[\mp \frac{\varepsilon_i(\vec{k})}{k_B T}\right] d\vec{k}}, \quad (1)$$

where the minus (plus) sign is for the electron (hole); $\tau(i, \vec{k})$ is the relaxation time; $\varepsilon_i(\vec{k})$ and $v(i, \vec{k})$ are the band energies and the component of the group velocity of the \vec{k} state of the i th band, respectively. The summation of the band was carried out over the VB for the hole and CB for the electron. Furthermore, the integration with respect to the \vec{k} states covers the first Brillouin zone (BZ).

In order to obtain the mobility, three key quantities ($\tau(i, \vec{k})$, $\varepsilon_i(\vec{k})$ and $v(i, \vec{k})$) must be determined. As the wavelengths of the thermally activated electrons or holes at room temperature in inorganic semiconductors, which are much larger than the lattice constant, are close to those of the acoustic phonon modes in the center of the first BZ, the electron-acoustic phonon coupling dominates the scattering at the low-energy regime,^{39–41} which can be calculated effectively by the deformation potential (DP) theory proposed by Bardeen and Shockley.⁵³ Accordingly, the relaxation time $\tau(i, \vec{k})$ based on the DP theory can be expressed as^{2,38}

$$\frac{1}{\tau(i, \vec{k})} = k_B T \frac{2\pi E_i^2}{\hbar C} \sum_{\vec{k}' \in \text{BZ}} \left\{ \left[1 - \frac{\vec{v}(i, \vec{k}')}{\vec{v}(i, \vec{k})} \right] \delta[\varepsilon(\vec{k}) - \varepsilon(\vec{k}')] \right\}. \quad (2)$$

Herein, the delta function implies that the scattering process is elastic and occurs between states with the same band index. E_i is the DP constant of the i -th band, and C is the elastic constant.

The band energy $\varepsilon_i(\vec{k})$ is calculated using the Vienna ab initio simulation package (VASP).⁵⁵ The \vec{k} -mesh is chosen as $1 \times 1 \times 300$ for the ribbons and $65 \times 65 \times 1$ for the sheets, which are fine enough to give converged relaxation times and mobilities. The generalized gradient approximation (GGA)⁵⁶ with the Perdew–Wang (PW91)⁵⁷ exchange correlation function is used with the plane-wave cutoff energy set at 400 eV for all calculations. The criterion of convergence is that the residual forces are less than $0.005 \text{ eV } \text{\AA}^{-1}$ and the change of the total energy is less than 10^{-6} eV . The vacuum space between the two adjacent NRs is set to be at least 10 \AA to eliminate the interactive effect between the two NRs. The group velocities of the electron and hole carriers can be obtained from the gradient of the band energy $\varepsilon_i(\vec{k})$ in \vec{k} -space, according to $v(i, \vec{k}) = \nabla \varepsilon_i(\vec{k})/\hbar$.

Results and discussion

The atomic structure of the material is shown in Fig. 1a. In order to illustrate the atomic arrangements for carrier conduction along the armchair (x) and zigzag (y) directions, an orthogonal supercell, which is covered by a green shadow box in Fig. 1a, is shown. The structure of an armchair ribbon is shown in Fig. 1b. We use the number of atomic chains (Na) to describe the width of the ribbon. Two types of edge modification were investigated: H atom termination (H-termination) and F atom termination (F-termination). The pristine ribbon is also investigated as a reference.

First, the electronic structure and the acoustic phonon-limited mobility in monolayer MoS₂ are investigated. In addition, the band structure and the first BZ of monolayer MoS₂ are shown in Fig. 2a and b, respectively. For monolayer MoS₂ sheets, the K point (with fractional reciprocal coordinates: $-1/3, 2/3$) defined in reciprocal lattice of the primitive cell is folded into the $(0, 1/3)$ point of the Γ – Ψ branch in the first BZ of the supercell (see Fig. 2b). There are two peaks around the top of the valence band but only one band valley around the bottom of the conduction bands. The band structure is the same as that in *Yongqing's* report.⁴²

The variation of the total energy (E) with a uniaxial strain (δ) applied along the x and y directions are shown in Fig. 2c. Based on these energy-strain curves, the in-plane stiffness, C^{2D} , can be obtained and the C^{2D} along the x and y directions are 131.311

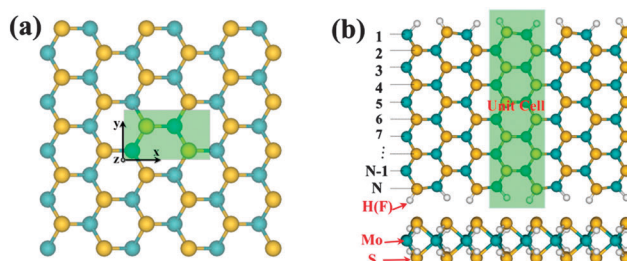


Fig. 1 Model of (a) MoS₂ sheet and (b) nanoribbons.

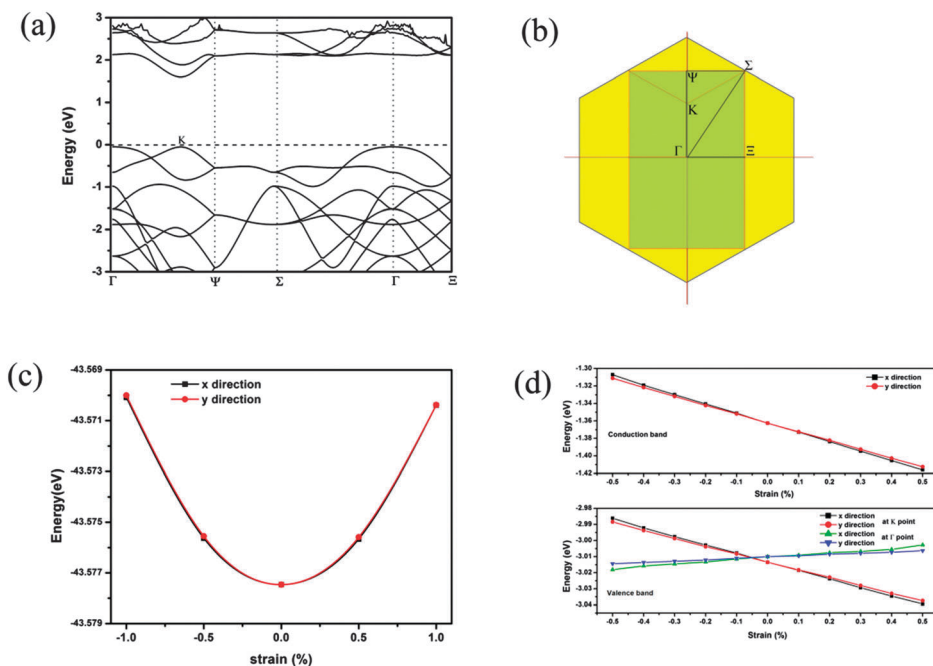


Fig. 2 Electronic properties of monolayer MoS₂ sheet. (a) Band structure for monolayer MoS₂ sheet with the orthogonal supercell shown in Fig. 1(a). (b) First Brillouin zone. (c) Energy–strain relationship along the x and y directions. (d) Shifts of the conduction band and valence band edges under a uniaxial strain.

and 131.473 N/m, respectively. The C^{2D} in our calculation are consistent with *Yongqing's* report (127.44 and 128.16 N/m). In general, the three-dimensional (3D) Young's modulus can be estimated as $C^{3D} = C^{2D}/t_0$. By assuming a finite thickness of ($t_0 = 0.65$ nm) for the 2D MoS₂ sheet, the Young's modulus amount are 202.02 and 202.27 GPa, respectively, which are in good agreement with the experimental value of 270 ± 100 GPa.^{58,59} Fig. 2d shows the shift of the band edges as a function of the strain along the x and y directions. Through dilating the lattice along the x and y directions, the DP constant E_1 is then calculated as $dE_{\text{edge}}/d\delta$, equivalent to the slope of the fitting lines, where E_{edge} denotes the energy of the conduction or valence band edge. For the conduction bands, there is just one band edge, which is located at the K point. The E_1 of electron along the x and y directions are -10.80 and -10.68 eV, respectively, which are the same as those reported by *Yongqing*.⁴² However, there are two band edges for the valance bands: one is located at the K point (the E_1 of hole along

the x and y directions are -5.28 and -5.22 eV, respectively, which is the same as that reported by *Yongqing*⁴²); the other is located at the Γ point (the E_1 along the x and y directions are 1.31 and 0.82 eV, respectively).

Based on the obtained energy-band spectrum, the values of E_1 and C^{2D} , the acoustic-phonon-limited relaxation time (using eqn (2)) and the mobility (using eqn (1)) at room temperature (300 K) are obtained, as shown in Table 1. The electron mobilities are 41.27 (the x direction) and 43.96 (the y direction) $\text{cm}^2 \text{V}^{-1} \text{s}^{-1}$. The hole mobilities are 96.62 (the x direction) and 64.19 (the y direction) $\text{cm}^2 \text{V}^{-1} \text{s}^{-1}$ for the K point, and 3079.39 (the x direction) and 4973.83 (the y direction) $\text{cm}^2 \text{V}^{-1} \text{s}^{-1}$ for the Γ point. If the BZ is divided into two parts: one includes the Γ point peak (signed as $\text{BZ}\Gamma$), and the other excludes the Γ point peak (signed as $\overline{\text{BZ}}\Gamma$, which includes K point peak). Thus, the total relaxation time (τ) can be determined as:

$$\frac{1}{\tau(i, \vec{k})} = k_B T \frac{2\pi E_i^2}{\hbar C} \sum_{\vec{k}' \in \text{BZ}\Gamma} \left\{ \left[1 - \frac{\vec{v}(i, \vec{k}')}{\vec{v}(i, \vec{k})} \right] \delta[\varepsilon(\vec{k}) - \varepsilon(\vec{k}')] \right\} + k_B T \frac{2\pi E_i^2}{\hbar C} \sum_{\vec{k}' \in \overline{\text{BZ}}\Gamma} \left\{ \left[1 - \frac{\vec{v}(i, \vec{k}')}{\vec{v}(i, \vec{k})} \right] \delta[\varepsilon(\vec{k}) - \varepsilon(\vec{k}')] \right\} = \frac{1}{\tau_\Gamma(i, \vec{k})} + \frac{1}{\tau_K(i, \vec{k})}. \quad (3)$$

We can obtain the total hole relaxation time, which equals τ_K . Following eqn (1), the hole mobility can then be obtained. The μ_h of an MoS₂ sheet are about 96.62 (the x direction) and 64.19 (the y direction) $\text{cm}^2 \text{V}^{-1} \text{s}^{-1}$. These values are smaller

Table 1 Deformation potential E_1 , in-plane stiffness C^{2D} , relaxation time τ , and mobility μ for electron (e) and hole (h) along the x and y directions in a 2D monolayer MoS₂ sheet at 300 K

Carrier type	Direction	E_1 (eV)	C^{2D} (N m ⁻¹)	τ (fs)	μ (cm ² V ⁻¹ s ⁻¹)	μ^* (cm ² V ⁻¹ s ⁻¹)
e	x	-10.80	131.31	14.88	41.27	72.16
	y	-10.68	131.47	15.22	43.96	60.32
h	x (K)	-5.28	131.31	52.15	96.62	200.53
	y (K)	-5.22	131.47	53.56	64.19	152.18
	x (Γ)	1.31	131.31	1229.16	3079.39	—
	y (Γ)	0.82	131.47	3125.25	4973.83	—

μ^* the mobility reported in ref. 42.

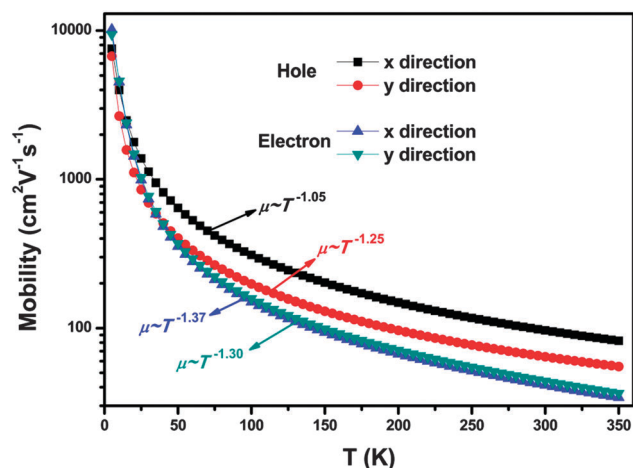


Fig. 3 Mobility as a function with temperature in MoS₂ sheet.

than the mobilities predicted by the effective mass method,⁴² owing to the greater number of band details considered in the BTE method. Our study shows that μ_e is about a half of μ_h . Our mobility results are in very good agreement with a recent indirect measurement based on the Hall effect for thin-flake MoS₂ reported by Zhang *et al.*⁶⁰ It showed that μ_h (86 cm² V⁻¹ s⁻¹) is twice the value of μ_e (44 cm² V⁻¹ s⁻¹).⁶⁰ Owing to the van der Waals interaction, the top of the valance band located at the *K* and Γ points in monolayer MoS₂ will shift to the Γ point in the multilayer material.⁶¹ Thus, the μ_h in the multilayer and bulk material will be mainly determined by the Γ points and is much larger than that of the monolayer material. In addition, the mobility as a function of temperature is shown in Fig. 3. It can be found that the mobilities of MoS₂ sheets decrease with a $T^{-\gamma}$ dependence with $\gamma = 1.05, 1.25, 1.37$ and 1.30 for the holes and electrons in the *x* and *y* directions, respectively. In the experiment, phonon scattering shows a weaker-than-expected temperature dependence ($\gamma = 0.55\text{--}0.78$) when the temperature is above ~ 100 K. But, when the temperature is above ~ 200 K, phonon scattering plays a major role in charge mobility, and mobility depends on T as $\mu \sim T^{-1.4}$,⁴⁶ which is in good agreement with our calculation.

In MoS₂ sheets, the states near the Γ point experience a strong interlayer coupling effect, as a result of the combination of the antibonding p_z -orbitals on the S atoms and d orbitals on the Mo atoms. Coming from the localized d orbitals on the Mo atoms, the states at the *K*-point are mainly located in the middle of the S–Mo–S sandwich structure and are relatively unaffected by interlayer coupling.⁶¹ In addition, there is a conduction valley located on the *K*-point, which is similar to graphene. In graphene, the electron at the *K*-point is considered as a quasi-free π electron, and the mobility can be up to 3×10^5 cm² V⁻¹ s⁻¹.³⁸ However, in the MoS₂ sheet, the π electron is located on Mo atoms and restricts the electron's movement. When the valance electron is excited to the conduction bands, there is a corresponding hole carrier. Owing to the fact that there are two valance band peaks, the hole carriers can be classified as the “ σ ” hole (located on Γ -point) and the “ π ” hole (located on *K*-point). In our calculation,

the “ σ ” hole can move much faster than the “ π ” hole. The reason can be found from the composition of the valance band. The valance band near the *K*-point is the combination of the d orbitals on the Mo atoms, which are bad for hole's movement. In addition, the valance band near the Γ -point is the combination of the antibonding p_z -orbitals on the S atoms and the d orbitals on the Mo atoms, which are good for the hole's movement. In MoS₂, the electron being excited at the *K* point is easier than that at the Γ point, owing to the direct gap at the *K* point. It then leads to the “ π ” hole being the major component of the hole. Because the mobility is always decided by the slower one, the migration speed of the “ π ” hole determines the mobility of an MoS₂ sheet.

Next, we investigate the μ of MoS₂ nanoribbons. As the zigzag MoS₂ nanoribbons are metallic, we herein only consider the semiconducting armchair MoS₂ nanoribbons, which are classified by the number of Mo–S dimer lines (*N*) across the ribbon width as shown in Fig. 1b. A series of armchair nanoribbons with widths in the range $7 \leq N \leq 16$ (from 1.0 to 2.4 nm) are calculated. It is well known that edge states exist in MoS₂ nanoflakes and dominate their catalytic performances. Thus, we expect that different edge modifications can affect the properties of the nanoribbons, and we therefore investigate the following three types of edge modification in the present study: pristine, H-termination and F-termination. The energy bands for these three edge modifications are shown in Fig. 4, in which it can be noted that there are the same deep energy bands. The differences in the band structures can be found between -0.3 and 1.5 eV. There are 10 bands (four valance bands and six conduction bands) for the pristine ribbon and four bands (two valance bands and two conduction bands) for the H-termination and F-termination ribbons, and the energy bands of the H-termination ribbon are similar to those of the pristine ribbon. Both of them are direct-gap semiconductors at the Γ points, and their energy gaps are oscillating around 0.55 eV with respect to the width. However, for the F-termination, the direct gap shifts to the *K* point, and the energy gap increases to about 0.95 eV.

For the 1D case, the stretching modulus is defined as $C^{1D} = [\partial^2 E / \partial \delta^2] / L_0$, where the uniaxial strain δ is applied along the ribbon direction, and L_0 is the lattice constant of the optimized ribbon, which is shown in Fig. 5a. Owing to the additional unpaired electrons, the Mo–S bonds at the ribbon edges are shorter than the bonds at ribbon's center, which lead to a small L_0 in pristine ribbons. For edges modified by H or F atoms, the L_0 is almost constant for different lattice lengths of the monolayer MoS₂ ribbon along the *x* direction (the black dashed line in Fig. 5a). Fig. 5b shows that C^{1D} increases continuously with *N* for all three types of ribbons. Considering the same width (W_0) for these three ribbons, the effective C^{2D} for the ribbon can be obtained as C^{1D} / W_0 , which is between 102.8 and 116.4 N m⁻¹ for pristine ribbons (between 100.7 and 113.6 N m⁻¹ for the H-termination and between 102.8 and 116.4 N m⁻¹ for the F-termination). Compared with the 2D sheet, the phonon spectrum of the nanoribbons broadens toward the high-frequency region, owing to the phonon mode quantization and the occurrence of edge phonon modes, which leads to the softening of the lattice modes and the reduction of the elastic modulus.⁴²

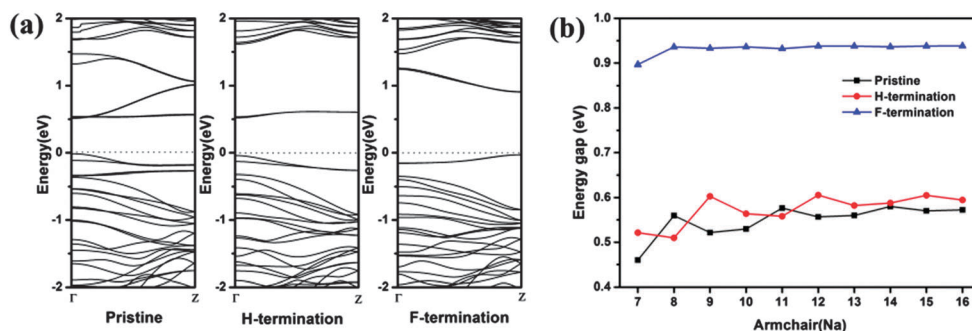


Fig. 4 (a) Band structure of an armchair nanoribbon ($N_a = 10$) and (b) the energy gap of an armchair nanoribbon as a function with width (N_a).

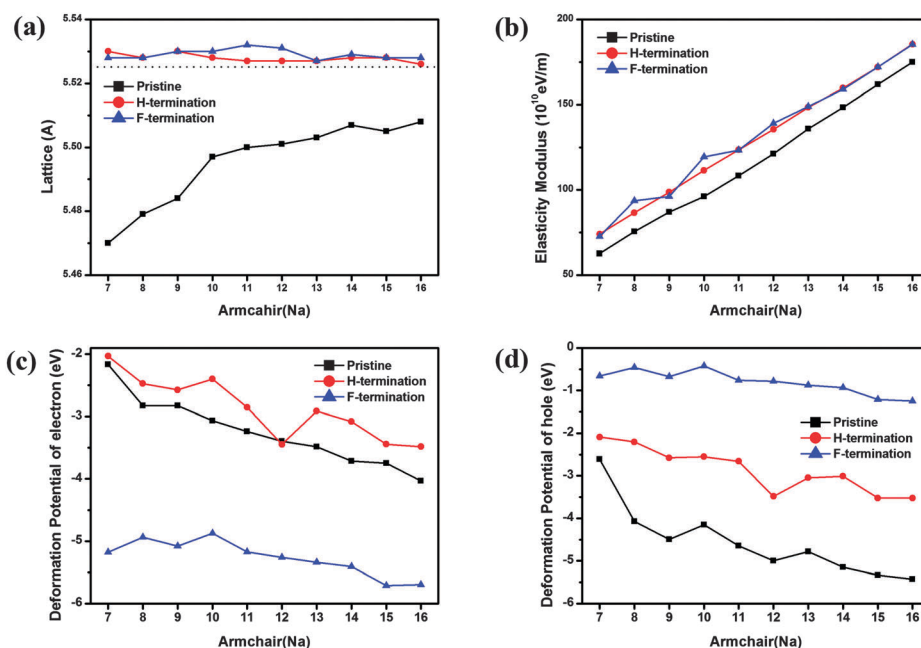


Fig. 5 (a) Lattice length, (b) elasticity modulus and deformation potential of (c) electron and (d) hole in armchair nanoribbons.

Fig. 5c and d show the DP constant E_1 of electrons and holes due to the quasi-static deformation of the ribbon. It can be noted that the $|E_1|$ of both electrons and holes are increasing with N for the three types of ribbons. For a specific N_a , the largest hole $|E_1|$ is found in the F-termination ribbons, which is about 2 eV higher than the pristine ribbons. The H-termination ribbons have the smallest hole $|E_1|$, which ranges between 2 eV and 3.5 eV. However, for the electron $|E_1|$, the smallest is in the F-termination ribbons, which is smaller than 1 eV; the largest is in the pristine ribbons, which is about twice of that of H-termination. $|E_1|$ of the hole is about five times larger than that of the electron in F-termination ribbons. In the pristine ribbon, $|E_1|$ of hole is about 1 eV larger than that of the electron. The difference of $|E_1|$ between electrons and holes is almost zero in H-termination ribbons. These results show that E_1 can be modified by edge modification in MoS_2 ribbons.

The room temperature μ for the ribbons are shown in Fig. 6, and the μ of the 2D sheet, represented by the horizontal dashed orange line, is also plotted for comparison. The μ_e and μ_h in

pristine ribbons, which oscillate between 25 and 35 $\text{cm}^2 \text{V}^{-1} \text{s}^{-1}$, respectively, vary with changing the width of the nanoribbons. The mobility in the H-termination ribbons initially oscillates with the width of the nanoribbons and then levels off to values of 44.80 and 93.95 $\text{cm}^2 \text{V}^{-1} \text{s}^{-1}$ for electrons and holes, respectively, which are close to the mobility of the 2D sheet (μ_e : 41.27 $\text{cm}^2 \text{V}^{-1} \text{s}^{-1}$ and μ_h : 96.62 $\text{cm}^2 \text{V}^{-1} \text{s}^{-1}$). The H-termination ribbons can be divided into three groups, which show smooth dependence on the width of ribbon N within each group. The first group includes ribbons with the ribbon width $N_a = 3p + 1$ (p is an integer), which has the largest μ_e . The $N_a = 3p + 2$ group has the largest μ_h , and the $3p$ group has the smallest μ_e and μ_h . The μ_e of F-termination ribbons moves close to that of the 2D sheet with an increase in the width of the nanoribbons. The μ_h in the F-termination ribbon initially can be above $10^3 \text{ cm}^2 \text{V}^{-1} \text{s}^{-1}$, with a maximum up to 2413.85 $\text{cm}^2 \text{V}^{-1} \text{s}^{-1}$; for some smaller ribbon widths < 11 , it then decreases with an increase in the width of the nanoribbons when the width is above 11. Nevertheless, the μ_h in the F-termination ribbons can still be as high as 425.20 $\text{cm}^2 \text{V}^{-1} \text{s}^{-1}$ (for $N_a = 16$).

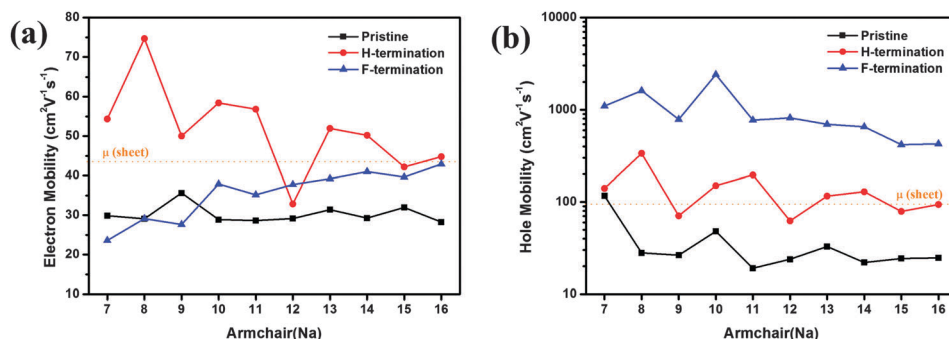


Fig. 6 Mobility of (a) electron and (b) hole in armchair nanoribbons. The dotted line is the mobility of monolayer MoS₂ predicted by the BTE method.

To understand the behavior of μ for different edge modifications in MoS₂ nanoribbons, we analyze the band-decomposed charge density at the edge of bands, as shown in Fig. 7. Because the same nanoribbons with the edge modification have a similar electronic character, the Na = 10 nanoribbon is chosen as representative for the analysis. It can be noted that the edge of the conduction bands is entirely located at the atoms of ribbon edges. The edge of valance bands is mainly located at the atoms of ribbon edges of pristine and H-termination ribbons and entirely located at the atoms of ribbon edges in F-termination ribbons. The band-decomposed charge density in the F-termination ribbons has mirror symmetry. For pristine ribbons, two valance bands (v_1 and v_2 in Fig. 7a) and four conduction bands (c_1 , c_2 , c_3 and c_4 in Fig. 7a) are considered. Atomic orbital analysis shows that all these states are mainly composed of Mo 4d manifolds, and the edge S atoms provide negligible contributions for the conduction bands (c_1 and c_2 in Fig. 7a). The conduction bands (c_1 and c_2 in Fig. 7a) are hybridization orbits with mixed 4d and 2p orbits. For the H-termination ribbons, the valance bands are similar to those in the pristine ribbons; the difference in the valance bands is that the plane states located at -0.25 to -0.3 eV (as shown in Fig. 4a), of which those states are composed of S 2p orbits in pristine ribbons, are not present in the H-termination ribbon. There are two conduction-degenerate bands (c_1 and c_2 in Fig. 7b) below 1.5 eV in the H-termination ribbons. In addition, atomic orbital analysis shows that the conduction bands are composed of Mo 4d manifolds (d_{yz} , d_{z^2} and $d_{x^2-y^2}$), S 2p and H 1s orbits. For F-termination, there are two double degenerate bands (v_1 , v_2 and c_1 , c_2 in Fig. 7c) around the Fermi level, and the atomic orbital analysis shows that F 2p manifolds account for an important proportion of all these states. Owing to the F 2p states, the electronic structures around the Fermi level brings a major change: The energy gap shifted from the Γ to the Z point.

From the band structure, we can find states near the Fermi level, which have parabolic dispersion. Thus, the effective mass (m^*) can be obtained by $\hbar^2[\partial^2\varepsilon(k)/\partial k^2]^{-1}$, as shown in Fig. 8a and b. The electron-effective mass initially oscillates with the width of the nanoribbons and then levels off to about $1.3 m_e$ (m_e is the mass of free electron) in the ribbons with three types of edge modifications. In the F-termination ribbons, the hole-effective mass also initially oscillates with the width of the nanoribbons

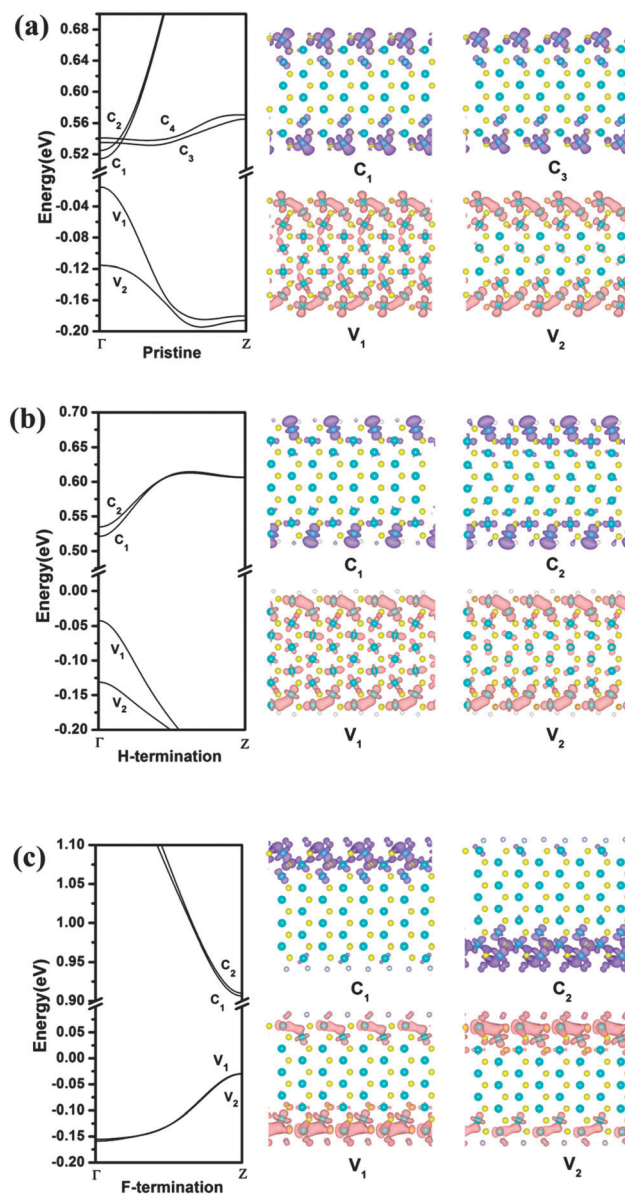


Fig. 7 Band-decomposed charge density of MoS₂ nanoribbons with Na = 10: (a) pristine ribbon; (b) H atoms termination ribbon; (c) F atoms termination ribbon. The Fermi level is set to zero.

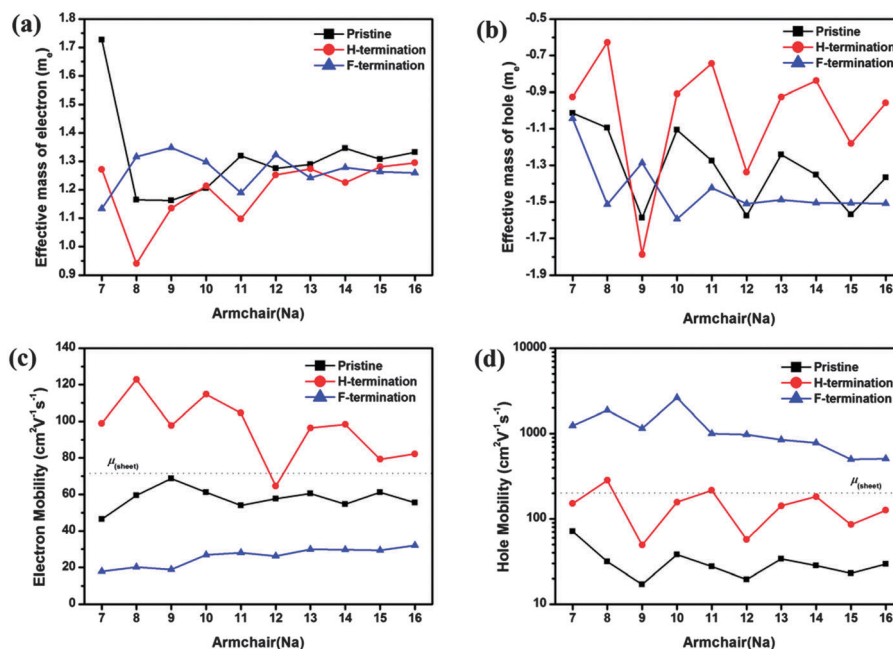


Fig. 8 Effective mass of MoS₂ ribbons and the mobility based on effective mass method: (a) effective mass of electron; (b) effective mass of hole; (c) the mobility of electron obtained by effective mass; (d) the mobility of hole obtained by effective mass. m_e is the mass of free electron. The dotted lines are the mobility of monolayer MoS₂, which are 72.16 (electron) and 200.52 (hole) $\text{cm}^2 \text{V}^{-1} \text{s}^{-1}$ as reported in ref. 42.

and then levels off to a value of $1.5 m_e$. There are three families of the hole-effective mass showing smooth trends within each family. The 3p family have the largest hole-effective

for the pristine and H-termination ribbons. The $3p + 2$ family have the smallest hole-effective mass for the H-termination ribbons, and the $3p + 1$ family have the smallest hole-effective

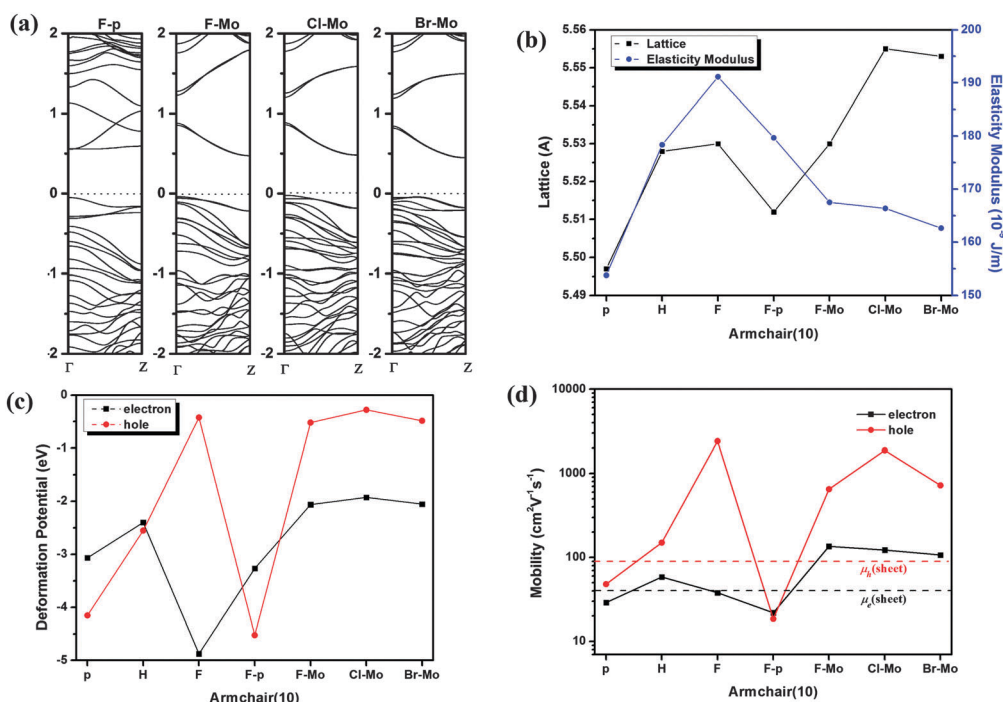


Fig. 9 (a) Band structures of armchair (10) with different edge modifications; (b) lattice length and elasticity modulus; (c) deformation potential (E_1); (d) mobility calculated by the BTE method. The pristine ribbon is denoted by p. Both of the two edges terminated by H atoms or F atoms are denoted by H or F. The ribbon with only one edge terminated by F atoms is marked as F-p. The model of only Mo atoms terminated by X (F, Cl and Br) atoms is denoted by X-Mo. The red (black) dashed line is the hole (electron) mobility of monolayer MoS₂ calculated by the BTE method.

mass for the pristine ribbons. The oscillatory behavior of the hole-effective mass gives rise to an oscillating μ_h . The mobility determined from the effective mass using the expression $\mu = e\hbar^2 C[(2\pi k_B T)^{1/2} |m^*|^{3/2} E_1^{-2}]^{-1}$ is shown in Fig. 8c and d. The μ_e in the pristine ribbon oscillates around $60 \text{ cm}^2 \text{ V}^{-1} \text{ s}^{-1}$, which is close to the μ_e in monolayer MoS_2 reported by Yongqing.⁴² The μ_h in the pristine ribbons has oscillations with a period of 3. The smallest mobility is found in the 3p family, and the largest is found in the 3p + 1 family. The μ_e of the H-termination ribbon initially oscillates with the width of the nanoribbons and then levels off to about $80 \text{ cm}^2 \text{ V}^{-1} \text{ s}^{-1}$. There are three families of μ_h in H-termination ribbons showing smooth trends within each family, with the 3p and 3p + 2 families having the smallest and largest mobilities, respectively. The μ_e in F-termination slowly increases from $20 \text{ cm}^2 \text{ V}^{-1} \text{ s}^{-1}$ to $30 \text{ cm}^2 \text{ V}^{-1} \text{ s}^{-1}$ with $7 \leq N \leq 16$. However, the μ_h in F-termination ribbons is up to about $10^3 \text{ cm}^2 \text{ V}^{-1} \text{ s}^{-1}$. The mobility predicted by the effective mass method is in agreement with that predicted by the BTE method, except for the μ_e in pristine ribbons, which are larger than that in F-termination. In a word, both the effective mass and BTE method suggest that the edge modification in MoS_2 ribbons can regulate the mobility.

From the mobilities of pristine, H-termination and F-termination systems, it can be found that the edge modification can regulate the electronic structures and charge mobilities. Considering the edge states play an important role in charge transport, the MoS_2 ribbon model of that one edge is terminated by F atoms, and the other kept pristine is investigated, which is denoted by F-p. In MoS_2 system, Mo atoms are donors, and S atoms are acceptors. The H atom's termination can maintain this relationship very well due to both of oxidability and reducibility in H atoms. However, F atoms have very strong oxidability. The S-F bond (-3.5835 eV) is much more difficult to form than the F-Mo bond (-5.262475 eV). The model that only Mo atoms are terminated by X (F, Cl and Br) atoms (denoted by X-Mo), is investigated. As shown in Fig. 9, for F-p, electronic properties are mainly dependent on the pristine edge. Thus, there are similar energy bands, in which deformation potential constants and mobilities can be observed. For X-Mo, there are indirect gaps in energy bands. The LUMO locates at the Z point, and HOMO locates at the Γ point. This is similar to the mixture of pristine and F-termination. The $|E_1|$ is obviously getting small when Mo atoms are terminated by X atoms. In X-Mo, the μ_e is calculated, reaching to $10^2 \text{ cm}^2 \text{ V}^{-1} \text{ s}^{-1}$, which is almost threefold of that in pristine ribbons and twofold of that in monolayer MoS_2 . The μ_h is calculated over $10^3 \text{ cm}^2 \text{ V}^{-1} \text{ s}^{-1}$, which is at least one order of magnitude larger than that in monolayer MoS_2 . These results suggest that the chemical modifications on the MoS_2 ribbon edge can change the energy bands and promote the carrier mobilities.

Conclusions

In summary, we have calculated the electronic structures and the intrinsic charge carrier mobilities of MoS_2 sheets and nanoribbons with the effect of a longitudinal acoustic phonon,

using the first-principles density functional theory and the BTE with the relaxation-time approximation. The numerical results indicate that the μ_h of a sheet at room temperature is about $96.62 \text{ cm}^2 \text{ V}^{-1} \text{ s}^{-1}$, which is twice that of μ_e ($43.96 \text{ cm}^2 \text{ V}^{-1} \text{ s}^{-1}$), whereas for the MoS_2 nanoribbons, the charge mobilities will be obviously decreased. The μ_e is about $30 \text{ cm}^2 \text{ V}^{-1} \text{ s}^{-1}$, and μ_h is about $25 \text{ cm}^2 \text{ V}^{-1} \text{ s}^{-1}$. Furthermore, we find that the edge modification can enhance the mobilities in nanoribbons. The mobilities in H-termination nanoribbons are about 45 (electron) and 95 (hole) $\text{cm}^2 \text{ V}^{-1} \text{ s}^{-1}$ and comparable to those in MoS_2 sheets. When edges are terminated by F atoms, the energy bands around the Fermi level are seriously changed, owing to the additional p orbitals. The μ_e is $42.94 \text{ cm}^2 \text{ V}^{-1} \text{ s}^{-1}$ (for $N = 16$) and close to the results in MoS_2 sheet and H-termination ribbons. The μ_h increases to $425.20 \text{ cm}^2 \text{ V}^{-1} \text{ s}^{-1}$ (for $N = 16$) rapidly, which is at least one order of magnitude larger than that in the pristine ribbons. In addition, when only the edge Mo atoms are terminated by halogen atoms, the μ_e will reach over $10^2 \text{ cm}^2 \text{ V}^{-1} \text{ s}^{-1}$, and the μ_h will reach over $10^3 \text{ cm}^2 \text{ V}^{-1} \text{ s}^{-1}$.

Acknowledgements

This work is supported by the National Natural Science Foundation of China (Grant No. 21103232, 61306149, and 11274260), the Natural Science Foundation of Hunan Province (No. 14JJ3026), the Hong Kong Scholars Program (No. XJ2013003) and the Shenghua Lieying Scholarship by the Central South University. It is also supported by Hunan Key Laboratory for Super-microstructure and Ultrafast Process and the Research Grants Council of Hong Kong SAR (Project No. CityU 100311/11P).

References

- 1 A. K. Geim and K. S. Novoselov, *Nat. Mater.*, 2007, **6**, 183–191.
- 2 M. Long, L. Tang, D. Wang, Y. Li and Z. Shuai, *ACS Nano*, 2011, **5**, 2593–2600.
- 3 D. Jose and A. Datta, *Acc. Chem. Res.*, 2014, **47**, 593–602.
- 4 M. P. Levendorf, C.-J. Kim, L. Brown, P. Y. Huang, R. W. Havener, D. A. Muller and J. Park, *Nature*, 2012, **488**, 627–632.
- 5 V. Mohan and A. Datta, *J. Phys. Chem. Lett.*, 2010, **1**, 136–140.
- 6 D. Jose and A. Datta, *Phys. Chem. Chem. Phys.*, 2011, **13**, 7304–7311.
- 7 M. Tahir and U. Schwingenschlogl, *Sci. Rep.*, 2013, **3**, 1075.
- 8 S. M. Jung, H. Y. Jung, M. S. Dresselhaus, Y. J. Jung and J. Kong, *Sci. Rep.*, 2012, **2**, 849.
- 9 Q. H. Wang, K. Kalantar-Zadeh, A. Kis, J. N. Coleman and M. S. Strano, *Nat. Nanotechnol.*, 2012, **7**, 699–712.
- 10 S. Yang, D. Li, T. Zhang, Z. Tao and J. Chen, *J. Phys. Chem. C*, 2012, **116**, 1307–1312.
- 11 Y. V. Joshi, P. Ghosh, P. S. Venkataraman, W. N. Delgass and K. T. Thomson, *J. Phys. Chem. C*, 2009, **113**, 9698–9709.
- 12 M. Remskar, A. Mrzel, M. Virsek, M. Godec, M. Krause, A. Kolitsch, A. Singh and A. Seabaugh, *Nanoscale Res. Lett.*, 2010, **6**, 26.

- 13 B. Radisavljevic, A. Radenovic, J. Brivio, V. Giacometti and A. Kis, *Nat. Nanotechnol.*, 2011, **6**, 147–150.
- 14 S. Kim, A. Konar, W. S. Hwang, J. H. Lee, J. Lee, J. Yang, C. Jung, H. Kim, J. B. Yoo, J. Y. Choi, Y. W. Jin, S. Y. Lee, D. Jena, W. Choi and K. Kim, *Nat. Commun.*, 2012, **3**, 1011.
- 15 C. Zhang, Z. Ning, Y. Liu, T. Xu, Y. Gao, A. Zak, Z. Zhang, S. Wang, R. Tenne and Q. Chen, *Appl. Phys. Lett.*, 2012, **101**, 113112.
- 16 F. L. Deepak, A. Mayoral and M. J. Yacaman, *Mater. Chem. Phys.*, 2009, **118**, 392–397.
- 17 F. L. Deepak, A. Mayoral, A. J. Steveson, S. Mejia-Rosales, D. A. Blom and M. Jose-Yacaman, *Nanoscale*, 2010, **2**, 2286–2293.
- 18 R. Kreizman, A. N. Enyashin, F. L. Deepak, A. Albu-Yaron, R. Popovitz-Biro, G. Seifert and R. Tenne, *Adv. Funct. Mater.*, 2010, **20**, 2459–2468.
- 19 G. Cunningham, M. Lotya, N. McEvoy, G. S. Duesberg, P. Schoot and J. N. Coleman, *Nanoscale*, 2012, **4**, 6260–6264.
- 20 L. Houben, A. N. Enyashin, Y. Feldman, R. Rosentsveig, D. G. Stroppa and M. Bar-Sadan, *J. Phys. Chem. C*, 2012, **116**, 24350–24357.
- 21 M. Ghorbani-Asl, S. Borini, A. Kuc and T. Heine, *Phys. Rev. B: Condens. Matter Mater. Phys.*, 2013, **87**, 235434.
- 22 C. Ataca, M. Topsakal, E. Akturk and S. Ciraci, *J. Phys. Chem. C*, 2011, **115**, 16354–16361.
- 23 K. F. Mak, C. Lee, J. Hone, J. Shan and T. F. Heinz, *Phys. Rev. Lett.*, 2010, **105**, 136805.
- 24 S. K. Mahatha, K. D. Patel and K. S. Menon, *J. Phys.: Condens. Matter*, 2012, **24**, 475504.
- 25 D. Xiao, G. B. Liu, W. Feng, X. Xu and W. Yao, *Phys. Rev. Lett.*, 2012, **108**, 196802.
- 26 T. Cheiwchanchamnangij and W. R. L. Lambrecht, *Phys. Rev. B: Condens. Matter Mater. Phys.*, 2012, **85**, 205302.
- 27 Z. Y. Zhu, Y. C. Cheng and U. Schwingenschlogl, *Phys. Rev. B: Condens. Matter Mater. Phys.*, 2011, **84**, 153402.
- 28 G. Kioseoglou, A. T. Hanbicki, M. Currie, A. L. Friedman, D. Gunlycke and B. T. Jonker, *Appl. Phys. Lett.*, 2012, **101**, 221907.
- 29 K. F. Mak, K. He, J. Shan and T. F. Heinz, *Nat. Nanotechnol.*, 2012, **7**, 494–498.
- 30 H. Zeng, J. Dai, W. Yao, D. Xiao and X. Cui, *Nat. Nanotechnol.*, 2012, **7**, 490–493.
- 31 T. Cao, G. Wang, W. Han, H. Ye, C. Zhu, J. Shi, Q. Niu, P. Tan, E. Wang, B. Liu and J. Feng, *Nat. Commun.*, 2012, **3**, 887.
- 32 Z. Gong, G. B. Liu, H. Yu, D. Xiao, X. Cui, X. Xu and W. Yao, *Nat. Commun.*, 2013, **4**, 2053.
- 33 S. Wu, J. S. Ross, G. B. Liu, G. Aivazian, A. Jones, Z. Fei, W. Zhu, D. Xiao, W. Yao, D. Cobden and X. Xu, *Nat. Phys.*, 2013, **9**, 149–153.
- 34 M. Q. Long, L. Tang, D. Wang, L. J. Wang and Z. G. Shuai, *J. Am. Chem. Soc.*, 2009, **131**, 17728–17729.
- 35 S. Bruzzone and G. Fiori, *Appl. Phys. Lett.*, 2011, **99**, 222108.
- 36 B. Xu, Y. D. Xiao, J. Yin, X. G. Wan, K. Jiang, A. D. Li, D. Wu and Z. G. Liu, *Appl. Phys. Lett.*, 2010, **96**, 183108.
- 37 G. Wang, *Phys. Chem. Chem. Phys.*, 2011, **13**, 11939–11945.
- 38 J. Xi, M. Long, L. Tang, D. Wang and Z. Shuai, *Nanoscale*, 2012, **4**, 4348–4369.
- 39 K. Kaasbjerg, K. S. Thygesen and K. W. Jacobsen, *Phys. Rev. B: Condens. Matter Mater. Phys.*, 2012, **85**, 115317.
- 40 K. Kaasbjerg, K. S. Thygesen and A.-P. Jauho, *Phys. Rev. B: Condens. Matter Mater. Phys.*, 2013, **87**, 235312.
- 41 X. Li, J. T. Mullen, Z. Jin, K. M. Borysenko, M. B. Nardelli and K. W. Kim, *Phys. Rev. B: Condens. Matter Mater. Phys.*, 2013, **87**, 115418.
- 42 Y. Cai, Z. Gang and Y.-W. Zhang, *J. Am. Chem. Soc.*, 2014, **136**, 6269–6275.
- 43 R. Fivaz and E. Mooser, *Phys. Rev. B: Solid State*, 1976, **163**, 743–755.
- 44 K. S. Novoselov, D. Jiang, F. Schedin, T. J. Booth, V. V. Khotkevich, S. V. Morozov and A. K. Geim, *Proc. Natl. Acad. Sci. U. S. A.*, 2005, **102**, 10451–10453.
- 45 S. Najmaei, Z. Liu, W. Zhou, X. Zou, G. Shi, S. Lei, B. I. Yakobson, J.-C. Idrobo, P. M. Ajayan and J. Lou, *Nat. Mater.*, 2013, **12**, 754–759.
- 46 B. Radisavljevic and A. Kis, *Nat. Mater.*, 2013, **12**, 815–820.
- 47 D. J. Late, B. Liu, H. S. S. R. Matte, V. P. Dravid and C. N. R. Rao, *ACS Nano*, 2012, **6**, 5635–5641.
- 48 R. Wang, B. A. Ruzicka, N. Kumar, M. Z. Bellus, H.-Y. Chiu and H. Zhao, *Phys. Rev. B: Condens. Matter Mater. Phys.*, 2012, **86**, 045406.
- 49 J. Wang, R. Zhao, M. Yang, Z. Liu and Z. Liu, *J. Chem. Phys.*, 2013, **138**, 084701.
- 50 X. Liu, T. Xu, X. Wu, Z. Zhang, J. Yu, H. Qiu, J.-H. Hong, C.-H. Jin, J.-X. Li, X.-R. Wang, L.-T. Sun and W. Guo, *Nat. Commun.*, 2013, **4**, 1776.
- 51 J. Xiao, M. Long, X. Li, H. Xu, H. Huang and Y. Gao, *Sci. Rep.*, 2014, **4**, 4327.
- 52 G. Nan, X. Yang, L. Wang, Z. Shuai and Y. Zhao, *Phys. Rev. B: Condens. Matter Mater. Phys.*, 2009, **79**, 115203.
- 53 J. Bardeen and W. Shockley, *Phys. Rev.*, 1950, **80**, 72–80.
- 54 W.-Q. Deng and W. A. Goddard III, *J. Phys. Chem. B*, 2004, **108**, 8614–8621.
- 55 G. Kresse and J. Furthmüller, *Comput. Mater. Sci.*, 1996, **6**, 15–50.
- 56 J. P. Perdew, K. Burke and M. Ernzerhof, *Phys. Rev. Lett.*, 1996, **77**, 3865–3868.
- 57 J. P. Perdew and Y. Wang, *Phys. Rev. B: Condens. Matter Mater. Phys.*, 1992, **45**, 13244–13278.
- 58 S. Bertolazzi, J. Brivio and A. Kis, *ACS Nano*, 2011, **5**, 9703–9709.
- 59 A. Castellanos-Gomez, M. Poot, G. A. Steele, H. S. J. van der Zant, N. Agrait and G. Rubio-Bollinger, *Adv. Mater.*, 2012, **24**, 772–775.
- 60 Y. Zhang, J. Ye, Y. Matsushashi and Y. Iwasa, *Nano Lett.*, 2012, **12**, 1136–1140.
- 61 A. Splendiani, L. Sun, Y. Zhang, T. Li, J. Kim, C.-Y. Chim, G. Galli and F. Wang, *Nano Lett.*, 2010, **10**, 1271–1275.